Energy Storage Materials 24 (2020) 220–228

Contents lists available at ScienceDirect

Energy Storage Materials

journal homepage: www.elsevier.com/locate/ensm

# Ion dynamics in Al-Stabilized $Li_7La_3Zr_2O_{12}$ single crystals – Macroscopic transport and the elementary steps of ion hopping

Patrick Posch [a,*], Sarah Lunghammer [a], Stefan Berendts [b], Steffen Ganschow [c], Günther J. Redhammer [d], Alexandra Wilkening [a], Martin Lerch [b], Bernhard Gadermaier [a], Daniel Rettenwander [a], H. Martin R. Wilkening [a,**]

[a] Institute for Chemistry and Technology of Materials, Christian Doppler Laboratory for Lithium Batteries, Graz University of Technology (NAWI Graz), Graz, Austria
[b] Department of Chemistry, Berlin University of Technology, Berlin, Germany
[c] Leibniz-Institut für Kristallzüchtung (IKZ), Berlin, Germany
[d] Department of Chemistry and Physics of Materials, University of Salzburg, Salzburg, Austria

ARTICLE INFO

*Keywords:*
Garnets
Single crystal
NMR
Dynamics
Conductivity

ABSTRACT

$Li_7La_3Zr_2O_{12}$ (LLZO) garnet-type ceramics are considered as very promising candidates for solid electrolytes and have been extensively studied in the past few years. Several studies report on an increase in ionic conductivity by doping with ions, such as $Al^{3+}$ and $Ga^{3+}$, to stabilize the cubic modification of LLZO. Unfortunately, so far ion dynamics have mainly been studied using powdered samples. Such studies may suffer from chemical heterogeneities concerning Al distribution. Here, we took advantage of Al-stabilized LLZO single crystals to throw light on the elementary steps of ion hopping. We used $^7$Li nuclear magnetic resonance (NMR) spin-lattice relaxation measurements and conductivity spectroscopy to probe dynamic parameters from both a microscopic and macroscopic point of view. At 293 K the total conductivity turned out to be 0.082 mS cm$^{-1}$, which is remarkably good for LLZO exhibiting an Al-content of only 0.37 wt%. Most importantly, $^7$Li NMR spin-lock transients revealed two overlapping diffusion-induced processes. Overall, activation energies from spin-lock NMR excellently agree with that from conductivity measurements; both techniques yield values around 0.36 eV. The corresponding diffusion coefficients deduced from NMR and conductivity measurements almost coincide. The magnetic spin fluctuations sensed by NMR provide an in-depth look at the elementary jump processes, which can barely be revealed by macroscopic impedance spectroscopy providing average values. In particular, we were able to precisely measure the local hopping barrier (0.20 eV) characterizing forward-backward jumps between the sites 24*d* and 96*h*.

## 1. Introduction

By signing the Kyoto Protocol in 1999, 84 industrial nations agreed on subsequent reduction of greenhouse gas emissions [1]. Achieving these goals is accompanied by a drastic decrease of our annual fossil fuel consumption. One possibility to reduce such emissions is to store energy that is generated from renewable resources [2].

In recent decades, electrochemical energy storage devices have proven to be suitable candidates for this purpose [3]. It is envisaged that such devices will find applications in static power plants as well as in automotive industry and the aviation sector. Li-ion batteries (LiBs) belong to the so far leading products used in our daily life [4]. Improvements are, however, needed if we want to meet the current demands formulated by automotive industry [5,6]. Materials for commercial LiBs are continuously improved [7]. However, independent of their size and energy density, they may suffer from stability issues caused by flammable liquids used as electrolytes [8]. Solid electrolytes [9,10] may significantly improve both safety and lifespan of batteries using $Li^+$ [11] or even $Na^+$ [12] as ionic charge carriers.

To realize the next generation of Li batteries with ceramic electrolytes, battery research faces the request to explore electrochemically stable and non-flammable ceramics that feature high Li-ion conductivities [11,13]. Replacing aprotic liquid electrolytes will, however, only be successful if we have economically friendly ceramics at hand that offer

* Corresponding author.
** Corresponding author.
*E-mail addresses:* p.posch@tugraz.at (P. Posch), wilkening@tugraz.at (H.M.R. Wilkening).

https://doi.org/10.1016/j.ensm.2019.08.017
Received 18 March 2019; Received in revised form 15 August 2019; Accepted 26 August 2019
Available online 30 August 2019

ion conductivities comparable to that of liquids [14,15]. Combined with low activation energies for ionic transport such systems can be operated over a large temperature range. Most importantly, they will withstand higher temperatures than conventional batteries. Clearly, the most suitable candidates should also exhibit negligible electronic conductivity, high chemical stability and low area specific resistances at the electrolyte|electrode interfaces [16]. From the broad variety of different materials, garnet-type [17,18] electrolytes are regarded as the most promising ones for all-solid state LiBs.

Since the first report of Murugan et al. on $Li_7La_3Zr_2O_{12}$ (LLZO) garnet, which exhibited a room-temperature ionic conductivity in the order of $10^{-3}$ to $10^{-4}$ S cm$^{-1}$, the interest in garnet-type materials with cubic symmetry grew rapidly [14]. The ionic conductivity of the cubic form of LLZO is by two orders of magnitude higher than that of the tetragonal polymorph (space group $I4_1/acd$) [19–21]. Stabilization of cubic LLZO is possible by appropriate doping [22]. $Li_7La_3Zr_2O_{12}$ first prepared by Murugan et al. was stabilized by $Al^{3+}$ doping [14]. Depending on the dopants, such as $Al^{3+}$ or $Ga^{3+}$, cubic LLZO crystallizes with different symmetries (space groups $Ia3\,d$ and $I4\,3d$) [23]. Meanwhile a huge number of studies can be found in literature that deal with the question which dopants are best suited to achieve a high conductivity of the cubic form [17,18,21–25]. These studies also investigate the possibilities to substitute $La^{3+}$ and $Zr^{2+}$ by alio- and isovalent cations [22].

Aliovalent doping with $Al^{3+}$, *i.e.*, substitution of $3Li^+$ ions by one $Al^{3+}$ cation, became the most popular method to stabilize cubic-LLZO and to create Li-ion vacancies [26]. Together with $Li^+$ the aluminium ions occupy the tetrahedral 24*d* sites in an irregular manner [27]. As a consequence, cation and bond disorder is produced affecting the site preference of the Li ions. This effect is assumed to significantly boost ionic conductivity [28].

In a recent comparison, Wachter-Welzl et al. address the interaction between dopant quantity and synthesis conditions [29]. In numerous reports [22], aluminium contents range from 0.17 to 0.35 $Al^{3+}$ ions per formula unit (pfu). Nonetheless, conductivities peak around 0.2 pfu [29]. Furthermore, co-doping with Ta further enhances $Li^+$ ion dynamics by shifting the $Al^{3+}$ ions to 96*h* sites resulting in a reduction of $Li^+$ diffusion pathways blocked by the immobile $Al^{3+}$ ions [30]. Quite recently, we reported on a single long-range $Li^+$ ion transport process through the lattice of Al-free single crystalline $Li_6La_3ZrTaO_{12}$ [31].

While doping is known to severely affect the Li ion transport behaviour, the preparation conditions also seem to have an enormous impact on the properties of the final product. In 2014, an overview to which extent the properties of LLZO may vary has been presented by Thangadurai et al. [22]. Synthesis routes like field assisted sintering technique (FAST), hot isostatic pressing or sol-gel preparation lead to quite different dynamic properties of the resulting material [25,32,33]. This can mainly be attributed to the density of the material affecting grain boundary ionic conductivities. As shown by Kim et al., lower sample density leads to increased grain boundary resistance, and thus, lowers the overall conductivity of the material [34].

To understand the elementary steps of ion hopping in Al-stabilized LLZO independent of the preparation and post-preparation conditions we take advantage of single-crystalline, Czochralski-grown $Li_7La_3Zr_2O_{12}$. We used contactless $^7$Li nuclear-magnetic resonance (NMR) spectroscopy [20,31,35–41] to probe the electric and magnetic field fluctuations the Li spins are exposed to during self-diffusion. The resulting diffusion-induced $^7$Li NMR spin-lattice relaxation rates, if studied as a function of temperature, entail information on both local hopping processes as well as long-range ion transport [16,38,39]. Throwing light on the underlying diffusion mechanisms that govern fast translational Li ion dynamics in Al-stabilized LLZO is expected to assist in the design of improved LLZO ceramics [22]. We compare our NMR results with results from alternating current (AC) conductivity measurements [42], which are widely used to characterize long-range ion motions in solids [43–45]. This comparison helps us to describe the motional correlation functions [37] controlling the fast cation exchange processes in LLZO-type materials.

## 2. Experimental

### 2.1. Sample preparation and characterization

The Al-stabilized LLZO single-crystal was grown directly from the melt using the Czochralski method. The raw materials, $Li_2CO_3$ (5 N, Alfa Aesar), $La_2O_3$ (4N5, Treibacher Industrie AG), $Al_2O_3$ (4 N, HAM) and $ZrO_2$ (4 N, Johnson-Matthey Chemicals), were dried and afterwards mixed in a stoichiometric ratio. The powder was pressed isostatically at 2 kbar and calcined at 680 °C for 70 h. The so-obtained body was melted in an inductively heated iridium crucible. On top of the crucible an active afterheater closed by a ring disc was placed; this arrangement was embedded in ceramic alumina insulation. The process chamber was rinsed with 5 N nitrogen at a rate of 21 l/h. An iridium wire served as crystallization seed that was pulled with 1.5 mm h$^{-1}$ and rotated at 10 rpm. Inductively coupled plasma mass spectrometry (ICP-MS) showed that the aluminium concentration in our single crystal was $[Al]_S = 0.37$ wt.-%. Comparing this value with the aluminium amount in the initial melt, $[Al]_L = 0.92$ wt.-% gives a first estimate for the aluminium distribution coefficient during the crystallization of the garnet phase from the melt: $k_{Al} = [Al]_S/[Al]_L = 0.4$. The concentration of 0.37 wt.-% yields a chemical composition of the crystal of $Li_{6.46}Al_{0.15}La_3Zr_{1.95}O_{11.86}$. This formula is written such that it refers to 3 $La^{3+}$ ions per formula unit; it illustrates the Al:La:Zr ratio. The exact oxygen stoichiometry is, of course, difficult to obtain; it can directly lead to a change in Li content. Such a change in Li content can influence the overall ionic conductivity leading to somewhat lower values than reported in literature. Earlier reports have put emphasis on the influence of oxygen stoichiometry on Li content and, thus, Li ion conductivity [29,46,47].

Here, we characterized out single crystals (space group symmetry $Ia3\,d$) by X-ray diffraction (see also Fig. S1); information on crystal data, structure refinement, atomic coordinates, bond lengths and occupation factors are shown in the Supporting Information (SI) section (Tables S1–S3). Data from single X-ray diffraction at large $q$ values provide very good estimates of site occupation numbers and bond length even for Li. To our experience, these data are even superior to those from powder neutron diffraction. All the crystals investigated turned out to be single crystalline in nature and of good quality with sharp Bragg reflections. We found no evidence for any kinds of intergrowth or for diffuse streaks indicative for chemical inhomogeneity. Altogether, we have analyzed more than 15 small pieces, which were left over from cutting a larger single crystal. All pieces reveal almost the same lattice parameters. Furthermore, also optically there were no clouded regions or even small changes in color within the large crystal. Hence, from X-ray single diffraction we can safely conclude that the crystals investigated are homogeneous with respect to Al distribution.

One of the larger, slightly yellow crystals (EK_Al3, see Tables S1 to S3, SI) was cut into smaller pieces of approximately 5 mm × 5 mm × 1 mm. These pieces were polished with a Struers LaboPol-25 device equipped with 300, 800, 1200, 2400 grit SiC abrasive paper at a speed of 300 rpm. Two gold electrodes, with a thickness of approximately 100 nm, were applied on top and bottom of one sample by using a Leica sputter device. For static $^7$Li NMR measurements another sample (EK_Al3, see SI) with dimensions of 1 mm × 1 mm × 8 mm was polished and then fused in a Norell SEPR250S quartz tube with a length of approximately 1.5 cm.

### 2.2. AC conductivity measurements

A Novocontrol Concept 80 broadband dielectric spectrometer was used to investigate impedance properties at frequencies ranging from 10 MHz to 0.1 Hz. In order to reveal temperature dependent properties, the device is equipped with a QUATRO cryosystem (Novocontrol) to vary the temperature. Here, we recorded conductivity isotherms covering a temperature range from 173 K to 453 K. The cryostat works by

vaporization of liquid $N_2$ that is stored in a dewar vessel. A heating element is used to create a constant gas flow of $N_2$. This setup allows us to control the temperature inside the sample cell with an accuracy of ±0.1 K.

### 2.3. NMR measurements

$^7$Li spin-lattice relaxation NMR measurements were performed using an Avance III spectrometer connected to an Ultrashield 500-MHz wide-bore magnet with a nominal field of 11 T. Additionally, we used an Avance III spectrometer in combination with an Ultrashield 300-MHz magnet (7 T). The magnetic fields correspond to $^7$Li Larmor frequencies of $\omega_0/2\pi = 194$ MHz and 116 MHz, respectively. A ceramic probe head, constructed to withstand high temperatures, was used for all experiments. Depending on temperature, the $\pi/2$ pulse length varied from 2.4 up to 3.4 μs maintaining a constant power output of 200 W throughout the measurements. The well-known saturation recovery sequence was used to acquire spin-lattice relaxation rates $1/T_1$. We also performed so-called spin-lock spin-lattice relaxation NMR measurements to study the temperature dependence of $1/T_{1\rho}$. For this purpose we took advantage of the spin-lock pulse sequence introduced by Lowe and Ailion. The locking frequency $\omega_1/2\pi$ was set to 33.3 kHz.

## 3. Results and discussion

### 3.1. $^7$Li NMR motional line narrowing

The fastest method and, in most cases, the first step to probe Li ion dynamics in solid materials is the acquisition of $^7$Li NMR line spectra [36, 48–50], see Fig. 1.

$^7$Li is a spin-3/2 nucleus and consequently, as its quadrupole moment is small compared to those of other nuclei, the NMR signal of a single crystal is expected to be composed of a central line (spin quantum transition $+1/2 \leftrightarrow -1/2$) and two quadrupole satellites ($+1/2 \leftrightarrow +3/2$, $-1/2 \leftrightarrow -3/2$). In the case of a vanishing electric field gradient, because of cubic symmetry around the Li nucleus, the Zeeman energy levels remain, however, undisturbed and the three lines collapse to a single one.

Here, only at low temperatures, particularly at $T = 213$ K, we notice quadrupole intensities of rather weak intensities. The intensities of the lines do not change much even if we use spin echo experiments [35] to overcome receiver dead time effects. If we decrease the temperature down to 123 K the satellite intensities are smeared out leading to a broader distribution of intensities. These broad humps sharpen with increasing temperature as both magnetic dipole-dipole interactions and electric quadrupolar interactions become increasingly averaged (see below). Finally, distinct satellite lines show up. We attribute these signals to the electrically inequivalent Li ions sensing non-vanishing electric field gradients (EFGs). In cubic LLZO the $Li^+$ ions reside on 24*d* and 96*h* sites. Moreover, some of the ions sense the $Al^{3+}$ cations (24*d*) in their direct neighborhood. Full averaging of the EFGs is only seen at sufficiently high temperatures, *i.e.*, when the Li jump rate reaches values comparable to the quadrupolar splitting (50 kHz) [51]. Here, if temperatures up to 453 K are considered, they completely disappear.

The width of the *central* line is determined by homo- and heteronuclear spin interactions; in the case of $^7$Li, homonuclear dipole-dipole interactions play the dominant role. At sufficiently low temperatures, *i.e.*, at temperatures where the Li diffusivity is frozen with respect to the NMR time scale, the width reaches its largest value, $\Delta\nu_R$. For many materials, dipolar coupling leads to values in the order of 3–15 kHz [49]. The onset of diffusive motions with rates in the order of $10^3\ s^{-1}$, that is, hopping of Li ions between magnetic inequivalent (and equivalent) sites, causes the line to narrow due to averaging of the effective dipolar couplings. This effect is similar to that of Brownian motion in the liquid state. Hopping between electrically inequivalent sites results in the above-mentioned averaging of EFGs.

Here, the so-called rigid lattice regime of the $^7$Li NMR central line of single crystalline Al-LLZO is reached at 163 K. This regime features a constant line width $\Delta\nu_R$ of approximately 8.7 kHz, see Fig. 1 a). With increasing temperature the full width at half maximum (fwhm) of the NMR line continuously decreases, finally reaching a motionally narrowed line at 350 K. The change in fwhm shown in Fig. 1 a) follows the behavior predicted by Abragam [50,52,53]; it obeys the relationship

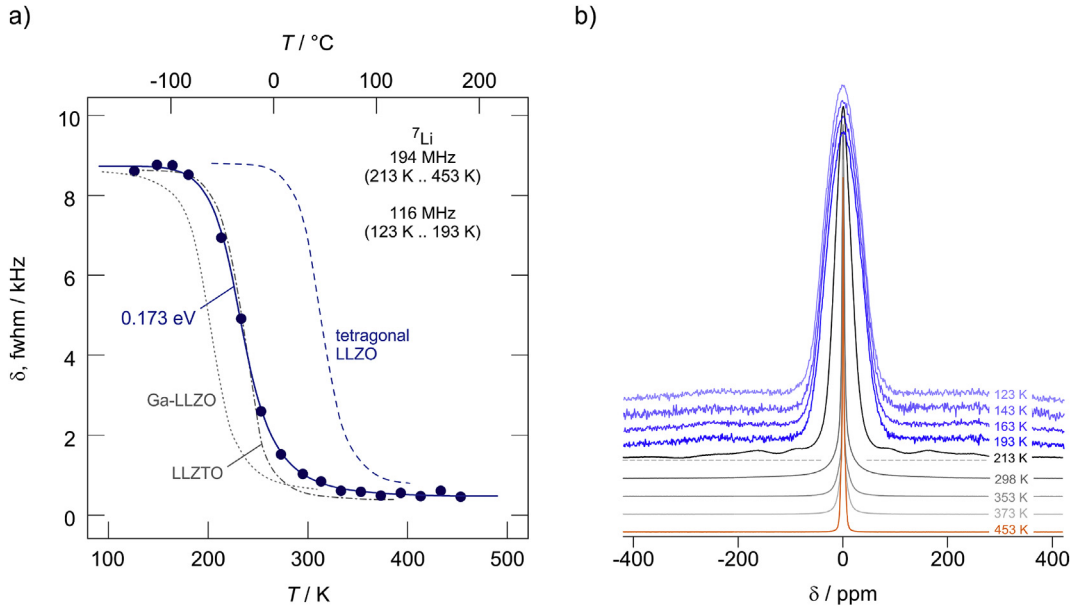


**Fig. 1.** a) $^7$Li NMR line narrowing of Al-stabilized $Li_7La_3Zr_2O_{12}$. Line widths (full width at half maximum, fwhm) have been determined from $^7$Li NMR spectra obtained with a single pulse experiment. The line width is independent of the external magnetic field used to acquire the spectra. To record lines at temperatures below 200 K we used a cryo-probe. The solid line represent a fit according to Abragam's formula to describe averaging of homonuclear dipole-dipole interactions. Dashed, dotted and dashed-dotted lines indicate the position of line narrowing curves of powdered tetragonal LLZO, powdered Ga-stabilized LLZO and $Li_6La_3ZrTaO_{12}$ (LLZTO) single crystals. b) $^7$Li NMR spectra of Al-stabilized LLZO single crystals recorded at the temperatures indicated; see text for further explanation. Again, at temperatures below 200 K spectra have been recorded at a Larmor frequency of 116 MHz.

$$\Delta\nu(T) = \Delta\nu_R \left[1 + \left(\frac{\Delta\nu_R}{B} - 1\right)\exp\left(\frac{E_{a,A}}{k_B T}\right)\right]^{-1} + D \quad (1)$$

which can be used to estimate a mean activation energy that governs motional line narrowing. $B$ is a fitting parameter and $k_B$ denotes Boltzmann's constant. Here, $E_{a,A}$ turned out to be in the order of 0.17 eV. This value perfectly agrees with that seen by $^7$Li NMR spin-lattice relaxation measurements, which were carried out in the laboratory frame of reference, see below.

At the inflexion point of the narrowing curve, the mean $Li^+$ jump rate ($\tau^{-1}$) is expected to be in the order of

$$\tau^{-1} = \Delta\nu_R \times 2\pi \quad (2)$$

With $\Delta\nu_R = 8.7$ kHz eqn. (1) yields a rate of $\tau^{-1} \approx 5.5 \times 10^4$ jumps per second at $T = 233$ K. The position of the whole narrowing curve of single crystalline Al-LLZO is highly comparable to that seen for $Li_6La_3ZrTaO_{12}$ single crystals (see the dashed-dotted line in Fig. 1 a)), which has been stabilized in its cubic form by replacing one half of the Zr (16*c*) ions by Ta. Both materials also exhibit very similar ionic conductivities. Although similar in shape and in $\Delta\nu_R$, the corresponding curve of polycrystalline, tetragonal $Li_7La_3Zr_2O_{12}$ [31], see the dashed line in Fig. 1 a), is shifted toward much higher temperature; the onset of line narrowing has been observed at $T = 280$ K pointing to the well-known difference in ion conductivity by a factor of 100 when compared with Al-stabilized LLZO. For comparison, also the motional narrowing curve of a Ga-stabilized LLZO powder sample has been included in Fig. 1a), see the dotted line. Depending on the kind and the amount of substituents, $Ga^{3+}$ or $Al^{3+}$, the onset of the line narrowing curve can be shifted down to temperatures as low as 150 K. Optimized garnet-type LLZO will then exhibit ionic conductivities of at least 1 mS cm$^{-1}$ at room temperature.

### 3.2. $^7$Li NMR spin-lattice relaxation rates

To shed further light on the underlying $Li^+$ diffusion mechanisms in Al-LLZO single crystal, we recorded diffusion-induced $^7$Li NMR spin-lattice relaxation rates ($1/T_1$), see Fig. 2 a). At low temperatures ($T < 250$ K), the $1/T_1$ rates recorded at $\omega_0/2\pi = 116$ MHz show a non-diffusive, *i.e.*, weaker-than-activated background regime (0.03 eV). All the magnetization transients, some of them are shown in Fig. 2 b), follow almost single exponential behavior. If we use stretched exponential to approximate longitudinal recovery, we found the stretching exponents $\gamma_1$ to take values very close to 1, see the upper graph of Fig. 2a). Above 280 K rates $1/T_1$ pass into the so-called low-temperature flank of the diffusion-induced rate peak $1/T_1(1/T)$ that shows up at $T_{max} = 500$ K. The activation energy $E_{a,NMR1}$ of the low-$T$ flank is 0.20(1) eV, the same value is, as expected, found for $1/T_1$ measured at a higher Larmor frequency of $\omega_0/2\pi = 194$ MHz. Most likely, $E_{a,NMR1}$ is to a large extent influenced by local $Li^+$ jump processes in the garnet structure. $Li^+$ ions jump have access to a 3D network of diffusion pathways generated by the 24*d* and 96*h* sites.

In the low-$T$ regime characterized by $\omega_0\tau_c \gg 1$, with $\tau_c$ being the motional correlation time, the rate $1/T_1$ depend on frequency. For 3D uncorrelated motion the model of Bloembergen, Purcell and Pound [39, 54] predicts $1/T_1 \propto \omega_0^{-\beta}$ with $\beta = 2$. As $\omega_0\tau_c \approx 1$ is valid at the temperature, $T_{max}$, at which the peak appears, the peak shifts toward higher $T$ the higher $\omega_0$ has been chosen. As with our setup we are limited in reaching temperatures above 500 K, we could only detect the peak maximum at a frequency of 116 MHz. According to $\omega_0\tau_c \approx 1$ we estimate that the mean $Li^+$ jump rate $1/\tau$, which is within a factor of 2 expected to be equal to $1/\tau_c$, is in the order of $7.3 \times 10^8$ s$^{-1}$.

Slower Li motional processes can be probed if $\omega_0$ is drastically reduced. Typically, the so-called spin-lock technique is applied to record diffusion-induced spin-lattice relaxation rates at frequencies in the kHz range. By using a locking frequency of 33 kHz the absolute rates increase

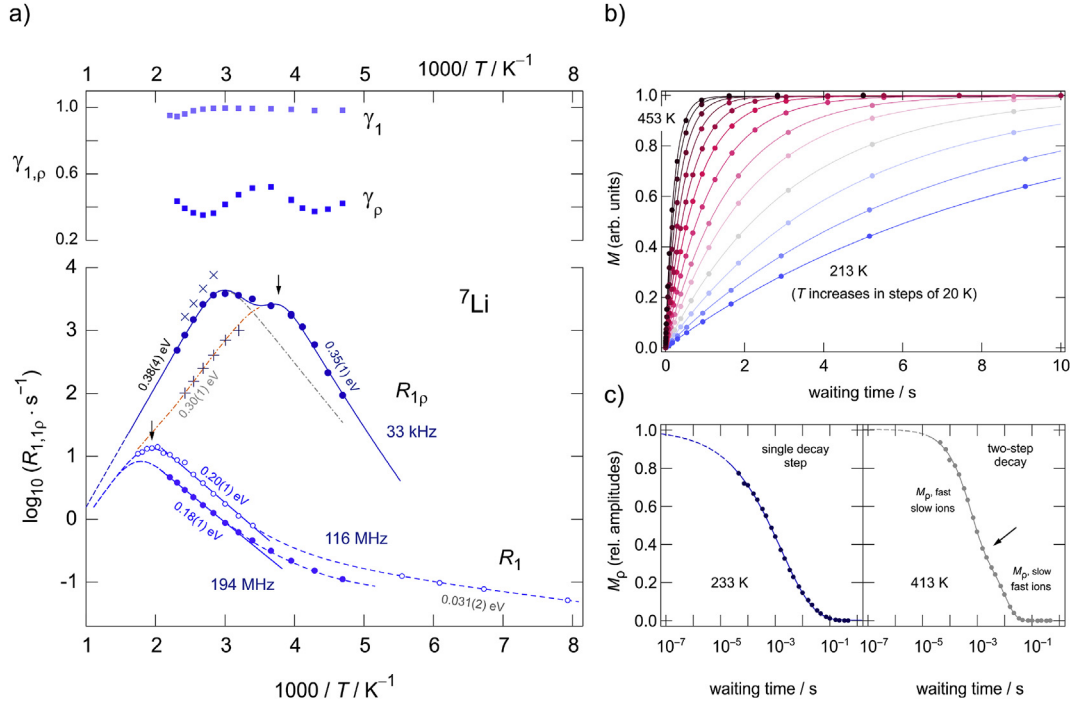


**Fig. 2.** a) $^7$Li NMR spin-lattice relaxation rates of single crystalline LLZO that were recorded in either the laboratory frame of reference $1/T_1 \equiv R_1$ (116 MHz and 194 MHz) or in the rotating frame of reference ($1/T_1 \equiv R_{1\rho}$ (33 kHz)). Dashed lines and dashed-dotted lines are to guide the eye. Solid lines show either Arrhenius fits ($R_1$) or are used as a guide to the eye to illustrate the temperature behaviour of the spin-lock $R_{1\rho}$ rates. We used either stretched exponential functions or a sum of two single exponential functions to parameterize longitudinal ($R_1$) and transversal relaxation ($R_{1\rho}$). In the upper graph, the corresponding stretching exponents, $\gamma_1$ and $\gamma_\rho$, are shown. In b) and c) selected magnetization transients $M$ and $M_\rho$ are depicted. Above room temperature the shape of $M_\rho$ is better described by a sum of two stretched exponentials. See text for further explanation.

and the peaks shift toward lower $T$. This change can be clearly seen in Fig. 2a). We recorded $1/T_{1\rho}$ rates at temperatures above 200 K; below this temperature we expect a similar non-diffusive regime as has been observed for $1/T_1$ (see above); see also our recent work on Li diffusion in $Li_{6.5}La_3Zr_{1.75}Mo_{0.25}O_{12}$. Here, if we parameterize the spin-lock magnetization transients with a single stretched exponential, we recognize that the corresponding rates $1/T_{1\rho}$ seem to pass through two relaxation peaks. A similar behavior has recently been observed also for polycrystalline $Li_{6.5}La_3Zr_{1.75}Mo_{0.25}O_{12}$. The peak at lower temperature, which appears at 265 K, reveals an activation energy of 0.35 eV in the low-$T$ regime. In contrast to $R_1$ (0.20 eV), relaxation in the presence of the much weaker spin-lock field is sensitive to long-range ion transport rather than to short-range motional processes in Al-stabilized LLZO. The value of 0.35 eV agrees with the activation energy seen by conductivity measurements which, *per se*, probe long-range ion transport. At $T_{max} = 265$ K the associated motional correlation jump rate can be calculated according to $\omega_1\tau_c \approx 0.5$; here we obtain $4.1 \times 10^5\ s^{-1}$.

Interestingly, careful inspection of the spin-lock transients shows that their shape can be best described with a two-step decay behavior. If we do so and use a sum of two stretched exponential functions to parameterize $M_\rho$, we obtain the rates shown by crosses in Fig. 2 a). Obviously, the rates $1/T_{1\rho}$ corresponding to the slower spin-lock relaxation process, marked as $M_{\rho,slow}$ in the two-step decay curve shown in Fig. 2 c), represent the high-temperature flank of the rate peak located at $T = 265$ K. Its high-$T$ activation energy of 0.3 eV points to an almost symmetric $1/T_{1\rho}(1/T)$ rate peak. Symmetric peaks, whose low-temperature flank is characterized by a slope not smaller than that in the high-$T$ regime ($\omega_1\tau_c \ll 1$), are expected for uncorrelated Li ion diffusion. If we extrapolate these rates to higher temperatures, we see that they almost coincide with those of the $1/T_1(1/T)$ peak recorded at 116 MHz. Hence, the $1/T_{1\rho}(1/T)$ peak showing up at 265 K corresponds to the peak seen by the laboratory-frame spin-lattice relaxation measurements.

The spin-lock peak seen at higher temperatures, viz. at $T = 336$ K, points to an activation energy of 0.38 eV. This value is similar to that seen by $T_{1\rho}$ NMR at low temperatures. The rates extracted from our analysis with two stretched exponentials agree well with the rates obtained if we simply use a single (stretched) exponential function. This agreement is because the amplitude of this fast relaxation process, $M_{\rho,fast}$, is larger than $M_{\rho,slow}$ (see Fig. 2 c)) and, thus, dominates the fitting results when analyzing the transients this way. While $M_{\rho,fast}$ is characterized by stretching exponents ranging from 0.75 to 0.82; the exponents for $M_{\rho,slow}$ range from 0.92 to 1. It is difficult to decide whether $M_{\rho,fast}$ is to a certain extent already influenced by transversal spin-spin relaxation. Nevertheless, $^7$Li NMR spin-spin relaxation is expected to be governed by the same activation energy as spin-lock relaxation in the regime $\omega_1\tau_c \ll 1$. Again, the activation energy of 0.38 eV, as seen in the limit $\omega_1\tau_c \ll 1$, reflects long-range Li ion transport in Al-stabilized $Li_7La_3Zr_2O_{12}$. This interpretation is supported by the fact that conductivity measurements on the same sample reveal a very similar value.

### 3.3. Conductivity measurements

In Fig. 3a) conductivity spectra $\sigma'(\nu)$ of Al-stabilized LLZO are shown. While electrode polarization dominates the electrical response at low temperatures and low frequencies, well-defined frequency independent plateaus show up at higher frequencies. From these plateaus, which are marked by arrows, we read off direct current ionic conductivities $\sigma_{DC}$ (see Fig. 4 b)).

Permittivity spectra (see Fig. 3 b)) and Nyquist plots (Fig. 4 a)) reveal that $\sigma_{DC}$ refers to capacitance values that are characteristic for bulk electrical relaxation processes. $\varepsilon'(\nu \to 0)$ shows values in the order of 100 as expected for bulk ion dynamics [55], see the dashed line in Fig. 3 b). The curvatures seen at frequencies lower than the main dc plateau, marked by a circle in Fig. 3 a), correspond to permittivities in the order of $10^5$. Thus, we do not attribute this response to bulk properties. As expected for such large permittivities (and capacitances) the corresponding peak in electric modulus spectra is reduced by a factor of $10^4$ compared to the main peaks shown in Fig. 3 c). Most likely, a small poorly conducting layer between the Au electrode and the LLZO single crystal, such as $Li_2CO_3$, is responsible for this response.

The $\sigma_{DC}$ plateaus pass into dispersive regions that roughly follow Jonscher's power law. Solid lines in Fig. 3 a) represent fits using $\sigma'(\nu) \propto \nu^p$ to approximate the frequency dependence in these regimes. At 193 K we obtained $p = 0.6$. Values ranging from 0.6 to 0.8 are typically expected for 3D motions of the charge carriers [56]. In general, dispersive regions are indicative for non-independent hopping of the ions [57]; furthermore, they point to time-scale dependent dynamic parameters. Here, at least at low temperatures, the ions are subjected to correlated motions involving the partly occupied 24*d* sites (occupation factor of

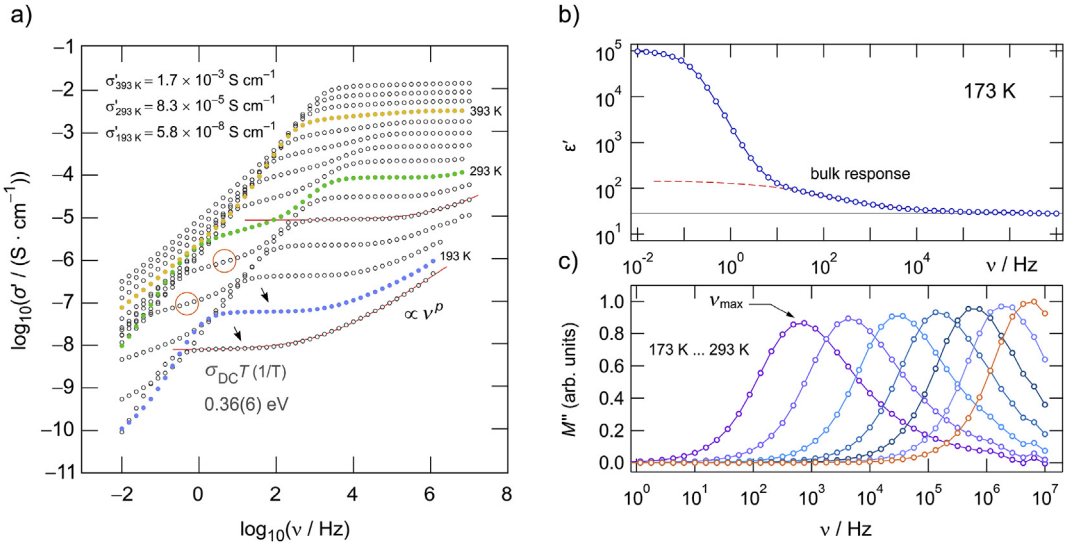


**Fig. 3.** a) Conductivity isotherms of single crystalline Al-stabilized $Li_7La_3Zr_2O_{12}$. Isotherms were constructed by plotting the real part $\sigma'$ of the complex conductivity versus frequency $\nu$. Solid lines show fits with Jonscher's power law; $p = 0.6$ indicates 3D Li diffusion. At room temperature the frequency independent conductivity plateau yields $8.3 \times 10^{-5}$ S cm$^{-1}$. b) Permittivity spectrum of Al-stabilized $Li_7La_3Zr_2O_{12}$ recorded at 173 K. c) Electric modulus spectra; the characteristic frequencies at the top of the peaks, if analyzed in terms of an Arrhenius diagram, reveal almost the same temperature dependence as $\sigma_{DC}$, see Fig. 5 b).

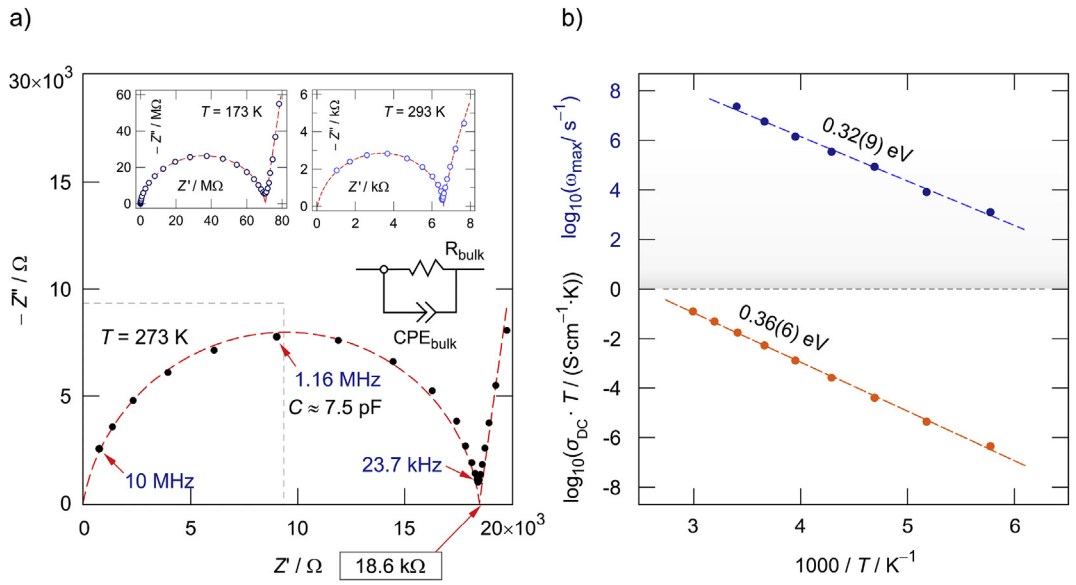


**Fig. 4.** a) Nyquist plots of Al-LLZO single crystals recorded at the temperatures indicated. Dashed lines show simulations with an equivalent circuit that is a combination of a resistor shunt with a CPE, depicted in the in the center section of the graph. b) Temperature dependence of $\sigma_{DC}T$ and $\omega_{max}$, extracted from conductivity spectra and electric modulus peaks. The dashed lines show linear fits following an Arrhenius law.

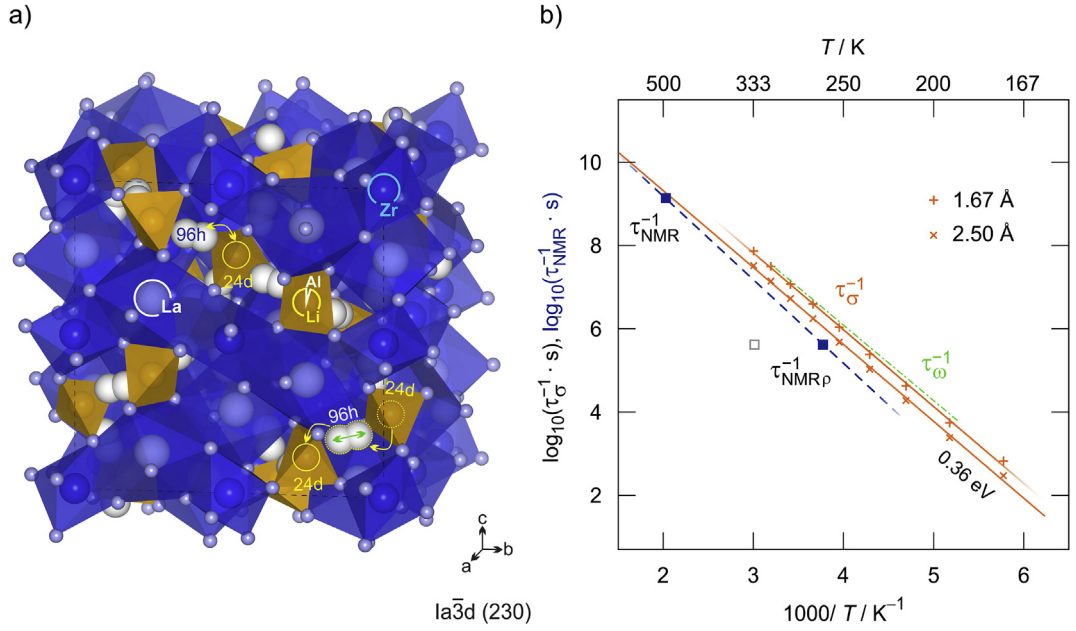


**Fig. 5.** a) Crystal structure of LLZO. The Li ions jump between the sites 24*d* and 96*h*. Also jumps directly between 96*h*, passing by the tetrahedral site 24*d*, which is partly occupied by the immobile $Al^{3+}$ ions, are indicated, see also Fig. 6 a) that shows possible $Li^{+}$ pathways in more detail. b) Li jump rates as deduced from conductivity and NMR spectroscopy. For comparison, characteristic hopping rates obtained from analyzing electric modulus spectra are also included; these rates have been indicated by the dashed-dotted line. $1/\tau_\sigma$ has either been calculated with $a = 1.67$ Å (+) or with $a = 2.50$ Å ( × ). The open symbol (■) refers to the $1/T_{1\rho}(1/T)$ NMR peak showing up at high temperatures.

approximately 0.58, see SI, Table S2 (EK_Al3)) and the 96*h* sites (occupation factor of ca. 0.34, see also SI, Table S2) sites in LLZO. It is likely that they sense a heterogeneous potential energy landscape and are exposed to forward-backward jump processes [57]. Thus, depending on the time scale the method used to study ion dynamics is sensitive to, different results for activation energies and jump rates are expected [43]. From this point of view it is possible to understand why also $R_1$ and $R_{1\rho}$, recorded either at frequencies in the MHz or kHz range, deliver quite different activation energies (0.2 eV ($R_1$) *vs.* 0.38 eV ($R_{1\rho}$)).

Dispersive regions in $\sigma'(\nu)$ result in (slightly) depressed semi-circles when impedance data are presented in a complex plane plot. In Fig. 4 a) the imaginary part, $-Z''$, of the complex impedance is plotted against its real part $Z'$. At the apex frequencies $\omega_a = 1/(RC)$ we estimate that the capacitance associated with the electrical response is given by $C = 7.5$ pF, $R$ denotes the resistance that can be determined from the intercept with the $Z'$ axis. Values in the pF range show that any contributions from gain boundary regions, which would be characterized by capacitances larger than 100 pF [55], are absent, as expected for a single crystal. Solid lines in Fig. 4 a) represent fits using an equivalent circuit consisting of the resistance $R$ connected in parallel to a constant phase element (CPE). The

shape of the curves in the Nyquist plots does not vary much with temperature. Thus, in the range of low temperatures no change in ionic transport process is seen by impedance spectroscopy.

At room temperature, the ionic conductivity is slightly lower than $10^{-4}$ S cm$^{-1}$ ($\sigma_{DC} = 8.3 \times 10^{-5}$ S cm$^{-1}$). Compared to values reported in the literature for Al-LLZO [22,58], this value is lower presumably because the amount of $Al^{3+}$ in our single crystal corresponds to only 0.15 mol per formula unit (pfu), as determined by ICP-MS. The optimal Al content to reach conductivities up to $10^{-3}$ S cm$^{-1}$ should be between 0.2 and 0.3 $Al^{3+}$ pfu. Moreover, also the Li content may influence the overall conductivity of our sample, as mentioned above. As we anticipate that most of the values presented in literature [22,29] refer to polycrystalline samples that could be affected by chemical inhomogeneities, a straightforward comparison of data from single crystals and powder samples is difficult. Regions with higher Al contents might act as percolating pathways ensuring an increase in long-range ion transport, while regions being low in Al concentration would hinder the ions to move over long distances. To determine the optimum Al content a series of Al-LLZO single crystals varying in Al content should be studied in the future.

In Fig. 5 b) the temperature dependence of $\sigma_{DC}T$ is shown. The activation energy of $E_{a,DC} = 0.36(6)$ eV is very similar to that seen by spin-lock ($R_{1\rho}$) NMR (0.35–0.38 eV, see above) showing that $^7$Li NMR spin-lattice relaxation if carried out in the rotating-frame of reference is able to probe long-range ion transport, as already mentioned above. Both, $\sigma_{DC}$ and $R_{1\rho}$ take advantage of a frequency window with values in the kHz region to sense the electrical and magnetic fluctuations associated with ionic transport. A very similar activation energy is also obtained if we analyze the temperature dependence of the characteristic relaxation frequencies from the electric modulus peaks of Fig. 3 b). In the upper graph of Fig. 4 the change of the rate $\omega_{max}$ (= $2\pi\ \nu_{max}$) with increasing temperature is shown in an Arrhenius diagram. The fact that $E_{a,DC}$ is a bit higher than $E_{a,M}$ points to a temperature dependent charge carrier concentration $N$. Obviously, $N$ slightly increases with increasing temperature.

### 3.4. Comparison of jump rates from NMR and with results from conductivity spectroscopy

To further compare our results from conductivity measurements with those from NMR relaxometry we converted $\sigma_{DC}$ into $Li^+$ jump rates using the Nernst-Einstein equation which connects $\sigma_{DC}$ with the solid-state diffusion coefficient $D_\sigma$ [16].

$$D_\sigma = \frac{\sigma_{DC} \cdot k_B T}{q^2 N} \tag{3}$$

where $q$ denotes the charge of the ions and $N$ the number density of the charge carriers. $D_\sigma$ is related to the macroscopic tracer diffusion coefficient via $D_\sigma = (1/H_R)\ D_t$. $D_t$ itself is linked to the self-diffusion coefficient $D$, which is available by NMR, according to $D_t = f\ D$. $H_R$ as well as $f$ represent the Haven ratio and the correlation factor, respectively [59]. With $D = D_{NMR} = a^2/(6\tau)$, where $a$ denotes the jump distance, we obtain

$$\tau^{-1} = (H_R / f)\ \frac{6\ k_B T}{q^2 N a^2} \sigma_{DC} \tag{4}$$

$1/\tau$ rates from either $\sigma_{DC}$ or NMR have been plotted vs. the inverse temperature in Fig. 5 b). If we first consider the jump rates only deduced from the maxima of the two relaxation rate peaks associated to each other, their position in Fig. 5 b) suggests an activation energy comparable to that seen by $\sigma_{DC}T$ (0.36 eV). Results from molecular dynamics simulations, suggesting concerted ion movements, agree with this value [60,61].

The rates $1/\tau_\sigma$ were calculated by assuming two different jump distances. If we use the 24*d*-96*h* distance of 1.67 Å the rates $1/\tau_\sigma$, if referenced to $1/\tau_{NMR}(T_1)$ are larger by a factor of $H_R/f = 0.44$ (≈0.5), pointing to correlated ionic motion. Agreement between $1/\tau_\sigma$ and $1/\tau_{NMR}(T_1)$ is achieved if $a$ is increased from 1.67 Å to 2.5 Å. The latter distance serves a good approximation to also include jumps performing 24*d*-[96*h*]-24*d* hopping processes and/or jumps between two 96*h* sites bypassing the 24*d* site (see below and Fig. 5 a) and Fig. 6 a)). The first pathway might also include the involvement of the 48*f* position in between the two 96*h* sites.

We also notice that $1/\tau_{NMR}(T_{1\rho})$ takes a value that is lower than expected by $1/\tau_{NMR}(T_1)$ and $1/\tau_\sigma$. This small difference can be explained by the influence of local magnetic fields that need to be taken into account when estimating $\tau_{NMR}$ via $\omega_1\tau_{NMR} = 0.5$ at the maximum of the $1/T_{1\rho}(1/T)$ peak. Replacing $\omega_1$ by an effective frequency $\omega_{eff} = 2\omega_1$ increases $1/\tau_{NMR}(T_{1\rho})$ such that $1/\tau_{NMR}$ agrees with $1/\tau_\sigma$ if calculated using $a = 2.5$ Å.

### 3.5. Diffusion pathways and assignment of activation energies

Coming back to the activation energies seen by NMR spin-lattice relaxation measurements, which range from 0.18 eV to 0.38 eV, and considering possible $Li^+$ diffusion pathways also discussed in the literature, we suggest the following assignment to the possible $Li^+$ jump processes in Al-LLZO. In LLZO, the $Li^+$ ions are distributed over the 24*d* and 96*h* sites. Here, our data on several single crystals did not reveal any evidences for additionally occupied $Li^+$ sites. From analyzing residual electron density maps we do not find any indications for Li on other positions (see also SI). This finding holds for the single crystal investigated here but also for samples prepared by sintering at temperatures as high as 1230 °C. Here, we do not find any indications that the 48*g* or any other site is regularly occupied. However, as mentioned above, the 48*g* site might act as a temporarily visited transition site when jumping between the 96 h sites. The 96*h* site is a so-called split-atom site; only one of the neighboring 96*h* sites is occupied by one $Li^+$ ion because of strong repulsive interactions. $Li^+$ moving in the 96*h*–96*h* (= [96*h*]) cage (see Fig. 5 a) and 6 a)) is presumably characterized by activation energies lower than 0.1 eV. This cage could also involve the 48*g* site connecting the 96*h* sites (96*h*-48*g*-96*h*′) Such localized motional processes might influence the $1/T_1$ rates governing spin-lattice relaxation at temperatures below 250 K, as suggested before.

The $1/T_1$ flank seen above 250 K is, however, assumed to reflect the hopping barrier connecting the sites 96*h* and 24*d* (Fig. 5 a) and 6 a)). The corresponding activation energy (0.18 eV–0.20 eV, 0.37 wt.-% $Al^{3+}$) is in good agreement with calculated values that have been presented in literature for Al-LLZO [62] or related structures [63].

If we compare activation energies extracted from the low-$T$ flank of the $1/T_1(1/T)$ NMR spin-lattice relaxation peaks of Al-LLZO powder samples with varying Al content, we see that lower activation energies (0.12 eV (0.9 wt.-% $Al^{3+}$) [19]; 0.13 eV (0.5 wt.-% $Al^{3+}$) [23]) are obtained for samples with higher amounts of $Al^{3+}$ ions. Hence, $Al^{3+}$ incorporation does not only stabilize the cubic crystal structure, it also seems to influence the mean activation energy of the elementary, local 24*d*-96*h* forward-backward jump process. However, this conclusion has to be taken with great care as powder samples prepared by sintering may suffer from chemical inhomogeneity. As has been shown recently for powdered samples, $Al^{3+}$ tends to heterogeneously distribute over the crystallites [29]. Such heterogeneous distribution has even been found inside the μm-sized grains. Here, for the dense single crystal investigated a homogenous distribution is present, as has been discussed above.

The activation energy seen by $1/T_{1\rho}$ measurements in the limit $\omega_1\tau_c \ll 1$ (0.3 eV) is expected to be governed by long-range transport processes, thus taking into account 24*d*-[96*h*]-24*d*′ hopping processes through the crystal lattice (Fig. 5a)). The activation energy of 0.3 eV agrees with those calculated for this type of pathway [64].

Even higher values ranging from 0.35 to 0.38 eV, which perfectly agree with $E_{a,DC}$, are anticipated to reflect similar exchange processes, which might additionally include further pathways characterized by somewhat higher barriers. Although still under debate, direct $Li^+$ jumps between two [96*h*] voids ($a = 0.234$ Å), using a curved pathway, might

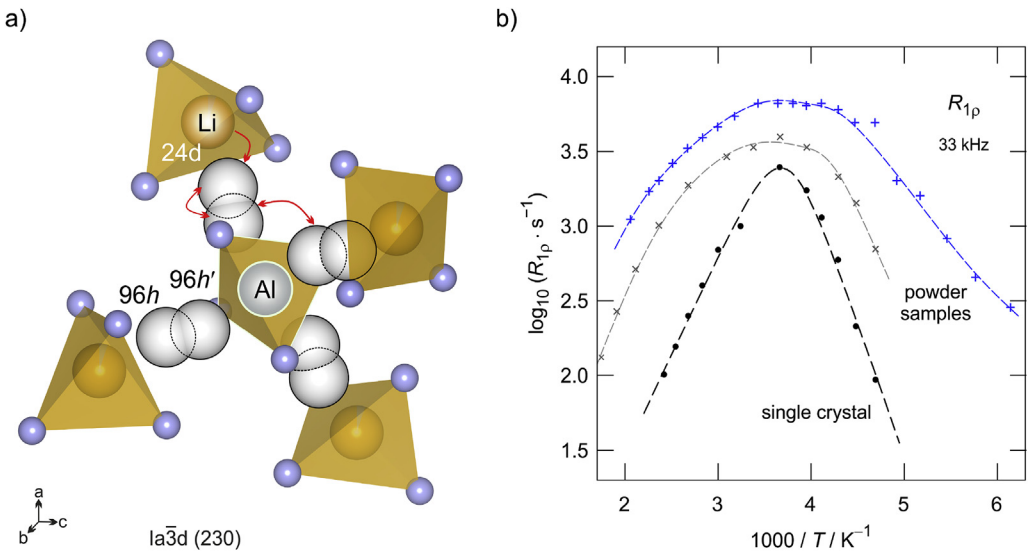


**Fig. 6.** a) $Li^+$ jump processes using the sites 24*d* and 96*h*. $Al^{3+}$ ions located at 24d block the pathway 96*h*-24*d*-96*h*. b) Comparison of diffusion-controlled $^7$Li NMR $1/T_{1\rho}$ rates of Al-LLZO powder samples (data points taken from Ref. [23] ( × , 0.49 wt.-% $Al^{3+}$) and ref. [19] (+, 0.9 wt.-% $Al^{3+}$)) with those measured in this study using a single crystal (0.37 wt.-% $Al^{3+}$). The extremely broad $1/T_{1\rho}(1/T)$ rate peak seen for powder samples is, most likely, due to a heterogeneous distribution of $Al^{3+}$ cations leading to a superposition of relaxation rate peaks.

contribute to the overall ion transport in Al-LLZO, too [62]. As has been shown recently by García Daza et al. [65] using molecular dynamic simulations, $Li^+$ diffusivity in the direct neighborhood of $Al^{3+}$ (see Fig. 6 a)) is decreased compared to the regions farther afield. They showed that vacancies, generated by trivalent doping, remain in the direct vicinity of $Al^{3+}$ without any effect in enhancing the $Li^+$ diffusivity of the adjacent $Li^+$ ions. We also suppose that the second $1/T_{1\rho}$ NMR peak yielding an activation energy of 0.38 eV reflects less mobile $Li^+$ ions that are indeed influenced by such a trapping or blocking effect of the $Al^{3+}$ ions. As $Al^{3+}$ is almost immobile with respect to the rapidly diffusing $Li^+$ ions, the pathway 24*d*-[96*h*]-$Al^{3+}$(24*d*)-[96*h*]-24*d* in its direct vicinity might be characterized by higher activation energies [66]. This blocking effect might force the ions to bypass the 24*d* position, thus directly jumping between two [96*h*] voids – possibly these jumps occur in the outer spheres of the pathways blocked by $Al^{3+}$. We assume that such blocking effects will lead to higher activation energies seen by conductivity spectroscopy as this method probes averaged values. NMR, on the other hand, is able to resolve the activation energies of the different jump processes in Al-LLZO.

### 3.6. Single crystals versus powder samples

Finally, we compare $^7$Li NMR $1/T_{1\rho}$ data from powder samples with that obtained in this study, see Fig. 6 b). It has been a mystery why the response in powders samples prepared by solid-state reaction always lead to an extremely broad $1/T_{1\rho}$ "peak" [19,23]. Most likely, chemical inhomogeneity concerning $Al^{3+}$ distribution, as mentioned above, leads to a superposition of several $1/T_{1\rho}(1/T)$ peaks hindering the very accurate determination of activation energies. For the single crystal studied here, this distribution is much smaller leading to sharp diffusion-induced $^7$Li NMR rate peaks.

Interestingly, heterogeneous $Al^{3+}$ distribution is only reflected in long-range ion dynamics, to which $T_{1\rho}$ NMR is sensitive. The shape of the $1/T_1(1/T)$ rate peaks, on the other hand, seem to be less influenced by the overall distribution of the trivalent cations.

## 4. Conclusions

Ion dynamics in Al-stabilized Czochralski-grown single crystals of the composition $Li_{6.46}Al_{0.15}La_3Zr_{1.95}O_{11.86}$ was studied by both $^7$Li NMR relaxometry, including line shape measurements, and broadband conductivity spectroscopy. As compared to powder samples, which are usually prepared by solid-state reaction and, thus, may suffer from chemical inhomogeneities, we benefit here from a highly dense sample whose $Al^{3+}$ distribution is assumed to be homogeneous. While conductivity spectroscopy probes long-range ion transport that is governed by an overall activation energy of 0.36 eV, $^7$Li NMR spin-lattice relaxation measurements provided details about activation energies (0.18 eV–0.38 eV) that describe both local barriers of the elementary jump processes and diffusion on a wider length scale. In particular, $Li^+$ exchange between the vacancy-rich crystallographic sites 24*d* and 96*h* turned out to be characterized by relatively low activation energies ranging from 0.18 eV to 0.20 eV. From an experimental point of view, we cannot exclude that also direct jumps between two neighboring 96*h*–96*h*′ voids bypassing the tetrahedral 24d sites do also participate in overall ion dynamics. Of course such jump processes occur less frequently in Al-LLZO and are expected to be characterized by higher activation energies.

## Acknowledgement

This project has received funding from the European Union's Horizon 2020 research and innovation programme under grant agreement no. 769929. Financial support by the Federal Ministry of Science, Research and Economy and the National Foundation for Research, Technology and Development (CD-Laboratory of Lithium Batteries: Ageing Effects, Technology and New Materials) is also gratefully acknowledged. Moreover, we thank NAWI Graz and the DFG for further financial support (WI3600, 2-1/4-1). Additional financial support by the FFG in the frame of the K-project 'safe battery' for financial support is also gratefully acknowledged.

## Appendix A. Supplementary data

Supplementary data to this article can be found online at https://doi.org/10.1016/j.ensm.2019.08.017.

## References

[1] U. Nations, United Nation 7 (1998) 214–217.
[2] D. Larcher, J.-M. Tarascon, Nat. Chem. 7 (2014) 19.
[3] M. Winter, R.J. Brodd, Chem. Rev. 104 (2004) 4245–4270.
[4] I. Buchmann, Batteries in a Portable World : A Handbook on Rechargeable Batteries for Non-engineers, second ed., Cadex Electronics Inc., Richmond, BC, Canada, 2001.
[5] M. Armand, J.-M.J.-M. Tarascon, Nature 451 (2008) 652–657.
[6] M.M. Thackeray, C. Wolverton, E.D. Isaacs, Energy Environ. Sci. 5 (2012) 7854–7863.
[7] S. Shi, J. Gao, Y. Liu, Y. Zhao, Q. Wu, W. Ju, C. Ouyang, R. Xiao, Chin. Phys. B 25 (2016) 018212.
[8] P.G. Balakrishnan, R. Ramesh, T. Prem Kumar, J. Power Sources 155 (2006) 401–414.

[9] F. Zheng, M. Kotobuki, S. Song, M.O. Lai, L. Lu, J. Power Sources 389 (2018) 198–213.
[10] J. Gao, Y.-S. Zhao, S.-Q. Shi, H. Li, Chin. Phys. B 25 (2016) 018211.
[11] Y. Kato, S. Hori, T. Saito, K. Suzuki, M. Hirayama, A. Mitsui, M. Yonemura, H. Iba, R. Kanno, Nat. Energy 1 (2016) 16030.
[12] A. Hayashi, K. Noi, A. Sakuda, M. Tatsumisago, Nat. Commun. 3 (2012) 856–860.
[13] Y. Wang, W.D. Richards, S.P. Ong, L.J. Miara, J.C. Kim, Y. Mo, G. Ceder, Nat. Mater. 14 (2015) 1026.
[14] R. Murugan, V. Thangadurai, W. Weppner, Angew. Chem. Int. Ed. 46 (2007) 7778–7781.
[15] N. Kamaya, K. Homma, Y. Yamakawa, M. Hirayama, R. Kanno, M. Yonemura, T. Kamiyama, Y. Kato, S. Hama, K. Kawamoto, A. Mitsui, Nat. Mater. 10 (2011) 682–686.
[16] M. Uitz, V. Epp, P. Bottke, M. Wilkening, J. Electroceram. 38 (2017) 142–156.
[17] V. Thangadurai, D. Pinzaru, S. Narayanan, A.K. Baral, J. Phys. Chem. Lett. 6 (2015) 292–299.
[18] S. Ohta, T. Kobayashi, J. Seki, T. Asaoka, J. Power Sources 202 (2012) 332–335.
[19] H. Buschmann, J. Dölle, S. Berendts, A. Kuhn, P. Bottke, M. Wilkening, P. Heitjans, A. Senyshyn, H. Ehrenberg, A. Lotnyk, V. Duppel, L. Kienle, J.J. Janek, J. Doelle, S. Berendts, A. Kuhn, P. Bottke, M. Wilkening, P. Heitjans, A. Senyshyn, H. Ehrenberg, A. Lotnyk, V. Duppel, L. Kienle, J.J. Janek, Phys. Chem. Chem. Phys. 13 (2011) 19378–19392.
[20] A. Kuhn, S. Narayanan, L. Spencer, G. Goward, V. Thangadurai, M. Wilkening, Phys. Rev. B Condens. Matter Mater. Phys. 83 (2011), 094302-1-094302-11.
[21] J. Awaka, N. Kijima, H. Hayakawa, J. Akimoto, J. Solid State Chem. 182 (2009) 2046–2052.
[22] V. Thangadurai, S. Narayanan, D. Pinzaru, Chem. Soc. Rev. 43 (2014) 4714–4727.
[23] R. Wagner, G.J.G.J. Redhammer, D. Rettenwander, A. Senyshyn, W. Schmidt, M. Wilkening, G. Amthauer, Chem. Mater. 28 (2016) 1861–1871.
[24] J.L. Allen, J. Wolfenstine, E. Rangasamy, J. Sakamoto, J. Power Sources 206 (2012) 315–319.
[25] E. Rangasamy, J. Wolfenstine, J. Sakamoto, Solid State Ion. 206 (2012) 28–32.
[26] D. Rettenwander, R. Wagner, J. Langer, M.E. Maier, M. Wilkening, G. Amthauer, Eur. J. Mineral. 28 (2016) 619–629.
[27] D. Rettenwander, J. Langer, W. Schmidt, C. Arrer, K.J. Harris, V. Terskikh, G.R. Goward, M. Wilkening, G. Amthauer, Chem. Mater. 27 (2015) 3135–3142.
[28] B. Kozinsky, S.A. Akhade, P. Hirel, A. Hashibon, C. Elsässer, P. Mehta, A. Logeat, U. Eisele, Phys. Rev. Lett. 116 (2016) 055901.
[29] A. Wachter-Welzl, J. Kirowitz, R. Wagner, S. Smetaczek, G.C. Brunauer, M. Bonta, D. Rettenwander, S. Taibl, A. Limbeck, G. Amthauer, J. Fleig, Solid State Ion. 319 (2018) 203–208.
[30] D.O. Shin, K. Oh, K.M. Kim, K.-Y. Park, B. Lee, Y.-G. Lee, K. Kang, Sci. Rep. 5 (2015) 18053.
[31] B. Stanje, D. Rettenwander, S. Breuer, M. Uitz, S. Berendts, M. Lerch, R. Uecker, G. Redhammer, I. Hanzu, M. Wilkening, Ann. Phys. 529 (2017) 1–9.
[32] I. Kokal, M. Somer, P.H.L. Notten, H.T. Hintzen, Solid State Ion. 185 (2011) 42–46.
[33] Y. Zhang, F. Chen, R. Tu, Q. Shen, L. Zhang, J. Power Sources 268 (2014) 960–964.
[34] Y. Kim, H. Jo, J.L. Allen, H. Choe, J. Wolfenstine, J. Sakamoto, J. Am. Ceram. Soc. 99 (2016) 1367–1374.
[35] V. Epp, Ö. Gün, H.-J. Deiseroth, M. Wilkening, Phys. Chem. Chem. Phys. 15 (2013) 7123–7132.
[36] V. Epp, Ö. Gün, H.-J.H.-J. Deiseroth, M. Wilkening, O. Guen, H.-J.H.-J. Deiseroth, M. Wilkening, J. Phys. Chem. Lett. 4 (2013) 2118–2123.
[37] P. Bottke, D. Rettenwander, W. Schmidt, G. Amthauer, M. Wilkening, Chem. Mater. 27 (2015) 6571–6582.
[38] A. Kuhn, M. Kunze, P. Sreeraj, H.D. Wiemhöfer, V. Thangadurai, M. Wilkening, P. Heitjans, H.-D. Wiemhoefer, V. Thangadurai, M. Wilkening, P. Heitjans, Solid State Nucl. Magn. Reson. 42 (2012) 2–8.
[39] M. Wilkening, P. Heitjans, ChemPhysChem 13 (2012) 53–65.
[40] M. Wilkening, W. Küchler, P. Heitjans, Phys. Rev. Lett. 97 (2006) 065901.
[41] I. Hanghofer, M. Brinek, S.L. Eisbacher, B. Bitschnau, M. Volck, V. Hennige, I. Hanzu, D. Rettenwander, H.M.R. Wilkening, Phys. Chem. Chem. Phys. 21 (2019) 8489–8507.
[42] S. Narayanan, V. Epp, M. Wilkening, V. Thangadurai, RSC Adv. 2 (2012) 2553–2561.
[43] F. Preishuber-Pflügl, P. Bottke, V. Pregartner, B. Bitschnau, M. Wilkening, Phys. Chem. Chem. Phys. 16 (2014) 9580–9590.
[44] S. Breuer, D. Prutsch, Q. Ma, V. Epp, F. Preishuber-Pflügl, F. Tietz, M. Wilkening, J. Mater. Chem. 3 (2015) 21343–21350.
[45] F. Preishuber-Pflügl, M. Wilkening, Dalton Trans. 43 (2014) 9901–9908.
[46] S. Smetaczek, A. Wachter-Welzl, R. Wagner, D. Rettenwander, G. Amthauer, L. Andrejs, S. Taibl, A. Limbeck, J. Fleig, J. Mater. Chem. 7 (2019) 6818–6831.
[47] M. Kubicek, A. Wachter-Welzl, D. Rettenwander, R. Wagner, S. Berendts, R. Uecker, G. Amthauer, H. Hutter, J. Fleig, Chem. Mater. 29 (2017) 7189–7196.
[48] M. Wilkening, V. Epp, A. Feldhoff, P. Heitjans, J. Phys. Chem. C 112 (2008) 9291–9300.
[49] M. Wilkening, S. Indris, P. Heitjans, Phys. Chem. Chem. Phys. 5 (2003) 2225–2231.
[50] D. Prutsch, B. Gadermaier, H. Brandstätter, V. Pregartner, B. Stanje, D. Wohlmuth, V. Epp, D. Rettenwander, I. Hanzu, H.M.R. Wilkening, Chem. Mater. 30 (2018) 7575–7586.
[51] R. Bertermann, W. Müller-Warmuth, Z. Naturforsch. Sect. A J. Phys. Sci. 53 (1998) 863–873.
[52] A. Abragam, The Principle of Nuclear Magnetism, Clarendon Press, Oxford, U.K., 1961.
[53] M. Wilkening, D. Bork, S. Indris, P. Heitjans, Phys. Chem. Chem. Phys. 4 (2002) 3246–3251.
[54] N. Bloembergen, E.M. Purcell, R. V Pound, Phys. Rev. 73 (1948) 679–712.
[55] J.T.S. Irvine, D.C. Sinclair, A.R. West, Adv. Mater. 2 (1990) 132–138.
[56] D.L. Sidebottom, Phys. Rev. Lett. 83 (1999) 983–986.
[57] K. Funke, C. Cramer, D. Wilmer, in: P. Heitjans, J. Kärger (Eds.), Diffus. Condens. Matter – Methods, Mater. Model., second ed., Springer, Berlin, 2005, pp. 857–893.
[58] P. Zhao, G. Cao, Z. Jin, H. Ming, Y. Wen, Y. Xu, X. Zhu, Y. Xiang, S. Zhang, Mater. Des. 139 (2018) 65–71.
[59] S. Lunghammer, D. Prutsch, S. Breuer, D. Rettenwander, I. Hanzu, Q. Ma, F. Tietz, H.M.R. Wilkening, Sci. Rep. 8 (2018) 11970.
[60] S. Adams, R.P. Rao, J. Mater. Chem. 22 (2012) 1426–1434.
[61] R. Jalem, Y. Yamamoto, H. Shiiba, M. Nakayama, H. Munakata, T. Kasuga, K. Kanamura, Chem. Mater. 25 (2013) 425–430.
[62] K. Meier, T. Laino, A. Curioni, J. Phys. Chem. C 118 (2014) 6668–6679.
[63] L.J. Miara, S.P. Ong, Y. Mo, W.D. Richards, Y. Park, J.-M. Lee, H.S. Lee, G. Ceder, Chem. Mater. 25 (2013) 3048–3055.
[64] M. Xu, M.S. Park, J.M. Lee, T.Y. Kim, Y.S. Park, E. Ma, Phys. Rev. B 85 (2012) 052301.
[65] F.A. García Daza, M.R. Bonilla, A. Llordés, J. Carrasco, E. Akhmatskaya, ACS Appl. Mater. Interfaces 11 (2019) 753–765.
[66] D. Rettenwander, P. Blaha, R. Laskowski, K. Schwarz, P. Bottke, M. Wilkening, C.A. Geiger, G. Amthauer, Chem. Mater. 26 (2014) 2617–2623.